Electrochimica Acta 513 (2025) 145529

Contents lists available at ScienceDirect

Electrochimica Acta

journal homepage: www.journals.elsevier.com/electrochimica-acta

Optimizing bimetallic NiRu@$Ti_3C_2T_x$ catalysts for oxygen evolution: The Impact of MXene content on Ru stability

Merve Buldu-Akturk [a,*], Thorsten Schultz [b,c], Namrata Sharma [d], Ursula Michalczik [e], Peter Bogdanoff [e], Norbert Koch [b,c], Michelle P. Browne [a,*]

[a] Helmholtz Young Investigator Group Electrocatalysis: Synthesis to Devices, Helmholtz-Zentrum Berlin für Materialien und Energie, 14109 Berlin, Germany
[b] Helmholtz-Zentrum Berlin für Materialien und Energie GmbH, 14109, Berlin, Germany
[c] Institut für Physik & IRIS Adlershof, Humboldt-Universität zu Berlin, Berlin, Germany
[d] Helmholtz-Zentrum Berlin für Materialien und Energie GmbH, Albert-Einstein-Straße 15, 12489 Berlin, Germany
[e] Institute for Solar Fuels, Helmholtz-Zentrum Berlin für Materialien und Energie GmbH, Hahn-Meitner-Platz 1, 14109 Berlin, Germany

ARTICLE INFO

Keywords:
Ruthenium leaching
Oxygen evolution reaction
MXene
Ti3C2Tx
NiRu

ABSTRACT

In this study, a bimetallic NiRu compound, synthesized by combining Ru with Ni and integrated it onto $Ti_3C_2T_x$ MXene surfaces at varying MXene contents (1 %–25 %) using a facile hydrothermal method were investigated for the Oxygen Evolution Reaction (OER). The NiRu@$Ti_3C_2T_x$ composites were evaluated in 1 M KOH electrolyte to assess how different MXene concentrations affect Ru stability and overall OER activity. Various characterization techniques were employed to analyze the morphological and microstructural properties of the synthesized pure and composite materials in order to elucidate the reasoning for the effect of the MXene on the Ru chemical stability and on the subsequent OER activity. We report that the incorporation of the bimetallic NiRu compound onto $Ti_3C_2T_x$ MXene surfaces at varying MXene contents significantly hindered the Ru leaching by maintaining the Ru oxidation state during oxygen evolution. The synthesized NiRu@MXene electrocatalysts demonstrated that MXenes can be utilized to stabilize the NiRu structure leading to less leaching of ionic and solid Ru species during the OER, while also delivering excellent OER activity.

1. Introduction

In light of the unprecedented impacts of the growing global population and industrialization on the planet Earth, regulations and policies have been implemented worldwide with the objective of supporting the increase of the global share of renewable energy at affordable prices. The production of green electricity from renewable sources, including hydropower, solar, wind, geothermal, and biomass, is of paramount importance for the sustainability of our planet. It is of equal importance, however, to ensure that electricity is utilized in an appropriate manner that does not contribute to atmospheric greenhouse gas emissions or other forms of pollution. Hydrogen (H_2) has been pointed out as the future's clean energy carrier with very low or net-zero emissions [1]. It is therefore of the utmost importance to develop water splitting technologies in order to produce green hydrogen in an efficient manner. Alkaline water electrolysis is a well-established and widely commercialized technology that offers the advantage of long-term stability at a lower cost when compared to the proton exchange membrane (PEM) electrolyzer.

In the field of water electrolysis research, the electrodes, namely the anode and the cathode, are the main focus of most of the ongoing research activities in this field, being the essential components of an electrolyzer stack where the electrochemical water splitting reactions take place. Two pH-dependent half-cell reactions take place during electrochemical water splitting at each electrode; the hydrogen evolution reaction (HER) by which hydrogen forms at the cathode, and the oxygen evolution reaction (OER) to form oxygen at the anode [2,3].

The OER is a multistep reaction that demands a greater energy input than that of HER due to the interaction of the intermediate species with the active catalyst surface to form O_2 in alkaline media. The sluggish kinetics of OH*, O* and HOO* adsorption results in OER being the rate-limiting step of the entire process, thereby increasing the overpotential [2]. With OER being the most challenging part, achieving high efficiency undoubtedly depends on the development of high-performance OER catalysts.

A variety of OER catalysts have been developed with the objective of

* Corresponding authors.
E-mail addresses: merve.aktuerk@helmholtz-berlin.de (M. Buldu-Akturk), michelle.browne@helmholtz-berlin.de (M.P. Browne).

https://doi.org/10.1016/j.electacta.2024.145529
Received 30 August 2024; Received in revised form 23 November 2024; Accepted 15 December 2024
Available online 16 December 2024

enhancing OER efficiency by accelerating the reaction kinetics. Platinum-group metals (PGM) and their oxides, especially iridium (Ir) and ruthenium (Ru)-based materials, are the state-of-the-art OER catalysts [4–6]. When considered separately by performance, IrO_2 possesses higher dissolution resistance while RuO_2 shows higher catalytic activity [7]. However, their large-scale industrial applications are constrained by their status as precious metals with low earth abundance, poor long-term stability and elevated cost. In particular, the leaching of Ru in alkaline media and its passivation in acidic media represents a significant challenge for its large-scale utilization [8,9]. Notable effort has been dedicated to the modification of Ir/Ru-based catalysts with the objective of enhancing their long-term stability, reducing the noble metal content while maintaining high efficiency, and developing non-noble metal-based catalysts with high OER efficiency [10–18]. Modifying the catalyst's crystal structure or surface is an effective strategy for enhancing its performance and stability, which can be done by i) nanostructuring to increase the active sites by increasing the surface area, ii) doping with inexpensive elements/species or iii) alloying with other metals [19].

Transition metal oxides (TMOs) have been widely studied as a great alternative for the replacement of PGM-based electrocatalysts, because they are inexpensive (compared to PGM-based electrocatalysts), tailorable and have multivalent oxidation states which makes them compatible with different oxidizing agents [18]. Yet, TMOs' low conductivity limits their effective use as OER catalyst. Other alternatives include hybrid or heterogeneous catalysts with different coordination environments, particle size, morphologies and dimensions, e.g., perovskites, layered double hydroxides, spinel structures, and metal chalcogenides [20–24]. Furthermore, carbon-based materials and, most recently, MXenes, have been investigated as 2D catalyst supports to boost the OER activity by providing a high surface area for the incorporation of the catalyst, which in turn increases the OER active surface area while reducing the amount of catalyst required to achieve the same degree of activity when compared to the bare material [25–29]. However, most bare MXene materials lack activity in OER due to the absence of late transition metals within its structure. Furthermore, $Ti_3C_2T_x$, the most commonly used MXene, rapidly transforms into TiO_2 during OER conditions, rendering it unsuitable as a bare catalyst for OER.

MXenes are a novel and rapidly advancing family of two-dimensional transition metal carbides and nitrides, with $Ti_3C_2T_x$ being the most commonly studied form. They are derived from a layered precursor material called the MAX phase, which is represented by the formula $M_{n+1}AX_n$. The MAX phase comprises an early transition metal (M), an A-group element (A) from groups 13–17 of the periodic table, and either carbon or nitrogen (X), the most common of which for the synthesis of $Ti_3C_2T_x$ is Ti_3AlC_2. The selective etching of Al layers in Ti_3AlC_2 can be achieved through the use of an aqueous solution of hydrofluoric acid (HF). This process results in the transformation of 3D crystalline Ti_3AlC_2 MAX phase particles into 2D Ti_3C_2 sheets. The surface titanium (Ti) atoms in these sheets are terminated with oxygen (–O), fluorine (–F), and hydroxyl (–OH) groups, which are denoted as T in the $Ti_3C_2T_x$ formula. >150 MAX phase compositions and 40 MXene compositions have been reported to date [30–32].

Numerous studies have been conducted on MXene-based materials for water splitting (i.e. HER and OER) [33–37]. Among these, OER represents a relatively novel and less-studied area compared to the HER [28,38–43]. Li *et al.* [33] demonstrated that the processes of phosphorization and MXene coupling in the NiFeCoP/MXene hybrid nanostructure could facilitate the formation of high-valence metallic elements, stimulate the formation of the NiOOH active phase at low voltage, and optimize the d-band center, which resulted in enhanced OER performance with an overpotential of 240 mV at 10 $mA\bullet cm^{-2}$, a Tafel slope of 55 $mV\bullet dec^{-1}$ and a long-term stability of 40 h in 1 M KOH electrolyte. Lu *et al.* [44] observed a 90 mV reduction in overpotential in the Co_3O_4/2D Ti_3C_2 MXene relative to its pure Co_3O_4 counterpart in 1 M KOH. The bimetallic RuCo-$Ti_3C_2T_x$ composites prepared by Yu *et al.* [45] exhibited an overpotential of 266 mV and a Tafel slope of 111.1 $mV\bullet dec^{-1}$ for the OER in 1 M KOH electrolyte.

However, in terms of metal/oxide stability there is lack of information on how MXenes would affect the stability of the metal/oxide in alkaline OER. In one study by Schmiedecke *et al.*, [38] a MXene material was shown to hinder the leaching of Cu from a CuCo material, which subsequently led to an increase in OER activity of the bi-metallic material by inductively coupled plasma optical emission spectroscopy (ICP-OES). Hence, in this study the investigation into the effect of MXene to enhance the stability of Ru-based catalysts (known for its heavy dissolution in alkaline media) in alkaline OER was carried out using this method. This is a significant challenge in the field that has yet to be extensively explored. Considerable effort has been put into the search for highly stable and efficient catalysts, mostly based on Ni, Fe, and Co, to replace the Ru- and Ir-based catalysts. However, the catalytic efficiencies of these materials still lack satisfactory performance.

More specifically, in this study, a bimetallic NiRu compound, which was incorporated onto the $Ti_3C_2T_x$ MXene surface at varying $Ti_3C_2T_x$ MXene contents (1 %–25 %) through a facile hydrothermal synthesis route, was prepared. The synthesized NiRu@$Ti_3C_2T_x$ composites were then investigated for OER in 1 M KOH electrolyte to explore the effect of the $Ti_3C_2T_x$ content on the stability and dissolution of Ru, as well as on the overall OER activity. A variety of techniques have been employed to characterize the synthesized pure and composite materials, in order to gain insight into the microstructure, morphological evolution, and chemical properties of the prepared catalysts.

2. Experimental

2.1. Chemicals and materials

Ti_3AlC_2 MAX phase (≤40 μm) was purchased from Carbon-Ukraine, hydrochloric acid (HCl, 37 %) and hydrofluoric acid (HF, 48 %, ACS reagent) were purchased from ROTH, and lithium chloride (LiCl, 99 %, extra pure) was purchased from ACROS organics. Sodium hydroxide (NaOH, 97+ %, ACS reagent) was purchased from Fisher Scientific. Ethylenediaminetetraacetic acid (EDTA, ACS reagent, 99.4–100.6 %), nickel (II) acetate tetrahydrate ($Ni(CH_3COO)_2{\cdot}4H_2O$, 99.995 %), ruthenium (III) chloride hydrate ($RuCl_3{\cdot}xH_2O$, ≥99.9 %), potassium hydroxide (KOH, ACS reagent, ≥85 %), and ethanol (≥99 %, reagent-grade) were purchased from Sigma-Aldrich. Nickel felt was purchased from Xinxiang AIDA Machinery Equipment Corporation, China. Ultra-pure water (18.2 $M\Omega\bullet cm^{-1}$) was used in all experiments. All chemicals were used as received without further purification.

2.2. Preparation of $Ti_3C_2T_x$

$Ti_3C_2T_x$ MXenes were prepared from the MAX phase Ti_3AlC_2 by wet chemical etching of Al layer in an aqueous mixture of HCl and HF. 1 g of Ti_3AlC_2 was etched in a 25 ml mixture of H_2O, HCl, and HF in a ratio of 3:6:1, respectively, by stirring at 35 °C for 24 h at 400 rpm in oil bath. The suspension was then washed 6 times by centrifugation at 3500 rpm (for 10 min at each centrifugation step) with approximately 1.5 L of ultra-pure water to bring down the pH of etched MXenes to 6–7. The delamination of multilayered $Ti_3C_2T_x$ MXenes was achieved by the intercalation of Li^+ ions by stirring the wet sediments in 50 ml of 0.5 M LiCl solution for 18 h at 400 rpm at room temperature. The suspension was then washed twice in ultra-pure water by centrifugation at 3500 rpm for 10 min each to remove excess Li^+ions. Finally, the dark-colored supernatant was collected from third wash as delaminated $Ti_3C_2T_x$ MXenes and then concentrated by centrifugation at 7500 rpm.

2.3. Synthesis of Ni- and Ru-based pure materials and their $Ti_3C_2T_x$ composites

NiRu@$Ti_3C_2T_x$ composites and their pure counterparts were synthesized through an EDTA-assisted hydrothermal synthesis route. For the synthesis of NiRu@$Ti_3C_2T_x$ composites, $Ni(CH_3COO)_2{\cdot}4H_2O$ (1 mmol) and $RuCl_3{\cdot}xH_2O$ (1 mmol) were first dissolved in an aqueous solution of EDTA (0.002 M) by continuous stirring for 15 min at room temperature under N_2 atmosphere in a glass beaker. Next, the required amount of colloidal $Ti_3C_2T_x$ solution (corresponding to the molar mass percentage) was added to the above solution and kept stirring for another 15 min at room temperature under N_2 atmosphere. The pH of the solution was then adjusted to 13–14 by adding NaOH. The solution was sonicated for 5 min in ice before being transferred to a Teflon-lined stainless-steel autoclave. The autoclave was then sealed and placed in an oven at 160 °C for 16 h. The autoclave was kept sealed until it naturally cooled down to room temperature. To remove the residual impurities, the product was collected and washed by centrifugation with deionized water and ethanol, each for 10 min and repeated three times. Finally, the product was dried overnight in an oven at 60 °C. The synthesized NiRu@$Ti_3C_2T_x$ composites were labelled as NiRu-1, NiRu-5, and NiRu-25 according to the $Ti_3C_2T_x$ molar mass percentages of 1, 5, and 25 %, respectively. The same synthesis procedure was followed for the synthesis of pure materials, represented as Ni, Ru and NiRu hereafter, excluding the addition of $Ti_3C_2T_x$.

2.4. Materials characterization

Powder X-ray diffraction (XRD) patterns were acquired using a Bruker D8 ADVANCE X-ray diffractometer with Cu Kα radiation (λ = 1.5418 Å) with a step size of 0.02° over a 2θ range from 5° to 90° at room temperature. Phase analysis was performed using Match! software and the patterns were identified using Inorganic Crystal Structure Database (ICSD) and the Crystallography Open Database (COD). The morphologies of the electrocatalysts were examined at an accelerating voltage of 1–2 kV using a Zeiss MERLIN Scanning Electron Microscope (SEM) equipped with a 0.1–30 keV field emission gun. X-ray photoelectron spectroscopy (XPS) measurements were conducted using a JEOL JPS-9030 setup with a base pressure of $2E^{-9}$ mbar. The powders were evenly distributed on carbon tape for the measurements. A non-monochromated Al source with 300 W power was used for excitation and a hemispherical analyzer with pass energy of 50 eV (surveys) and 20 eV (narrow scans) was used to detect the emitted photoelectrons. The binding energy scale of the analyzer was calibrated by setting the $Au4f_{7/2}$ and the $Cu2p_{3/2}$ peaks of clean gold and copper foils to 84.0 eV and 932.6 eV, respectively. However, since the samples showed charging, we shifted the binding energy of the C—C peak of the carbon tape to 285.0 eV for comparison. CasaXPS was used to fit the spectra [46]. The transmission electron microscopy (TEM) analyses were performed using an FEI Talos F200S instrument operated at 200 kV. The samples were prepared by dropping 30 μL of nanoparticle suspension onto a copper grid and allowing them to dry at room temperature. Energy-dispersive X-ray spectroscopy (EDX) equipped with two silicon drift detectors (SDD) was employed to analyze the elemental composition of the materials. ICP-OES measurements were performed using an iCAP 7400 Duo Full MFC device (Thermo Fisher Scientific) in axial mode.

2.5. Electrochemical measurements

All electrochemical experiments were carried out with a standard three-electrode system in a 1 M KOH solution using a Metrohm Autolab VIONIC potentiostat at room temperature. A catalyst-loaded nickel felt (NF) was used as the working electrode. The reference and counter electrodes were a mercury-mercury oxide (Hg/HgO) electrode (with a 1 M KOH internal solution) and a graphite rod, respectively. Prior to the three-electrode measurements, the 1 M KOH electrolyte was purged with N_2 for over 30 min. All measured potentials (vs. Hg/HgO) were converted to the reversible hydrogen electrode (RHE) according to the Nernst equation:

$$E_{RHE} = E_{Hg/HgO} + 0.059\ pH + E^0_{Hg/HgO} \tag{1}$$

where $E_{Hg/HgO}$ is the standard potential of the Hg/HgO electrode, which is 0.098 V at 25 °C.

Cyclic voltammetry (CV) was performed at a scan rate of 40 $mV{\cdot}s^{-1}$. Potentiostatic electrochemical impedance spectroscopy (PEIS) was carried out at a non-Faradaic potential over a frequency range of 100 kHz to 0.1 Hz with a perturbation of 10 mV. Linear sweep voltammetry (LSV) and Tafel slope measurements were conducted at a scan rate of 1 $mV{\cdot}s^{-1}$. Before the LSV measurements, three cycles of CV were performed to activate the catalyst. The stability tests were performed by conducting chronopotentiometry (CP) at a constant current density of 10 $mA{\bullet}cm^{-2}$ for 12 h. All reported data are presented in 90 % iR compensated form. Chronoamperometry was conducted at the initial potential of CV and LSV prior to each CV and LSV measurement until the catalysts reached a steady state.

To prepare the working electrode, a catalyst ink was prepared by dispersing 10 mg of catalyst powder in a solution containing 1 ml of deionized water/isopropanol (1:1) and 8 μL of Nafion solution. The catalyst ink was then continuously sonicated for 30 min to obtain a homogenous suspension. Finally, 150 μL catalyst ink was sprayed onto one side of the Ni felt with an exposed geometrical area of 1 cm^2 and dried at 50 °C on a hot plate. The uncoated end of the prepared working electrode was attached to a PTFE electrode holder equipped with a Pt sheet as a conductive material and dipped into the electrolyte. Prior to spraying the catalyst, NF was first sonicated in 35 % HCl for 10 min to remove oxide films from the surface, followed by sonication in acetone, ethanol, and deionized water for 15 min each before use.

3. Results and discussion

3.1. Morphological and microstructural characterization

The synthesis of NiRu@$Ti_3C_2T_x$ composites was achieved through a facile hydrothermal synthesis route, as illustrated in Fig. 1. Prior to the synthesis of NiRu@$Ti_3C_2T_x$, the $Ti_3C_2T_x$ was initially prepared through the etching of the MAX phase (Ti_3AlC_2) to remove the Al layer and produce multi-layer $Ti_3C_2T_x$. Subsequently, intercalation of $Li+$ with LiCl led to the formation of delaminated $Ti_3C_2T_x$. Thereafter, the synthesis of NiRu@$Ti_3C_2T_x$ composites was achieved by incorporating $Ti_3C_2T_x$ molar mass percentages of 1, 5, and 25 %, followed by heating in an autoclave at 160 °C for 16 h. Additionally, the pure counterparts of the composites, pure Ni, Ru and NiRu, were synthesized for the comparison. A detailed description of the synthesis procedure is provided in the experimental section. From here on, the synthesized NiRu@$Ti_3C_2T_x$ composites will be referred to as NiRu-1, NiRu-5, and NiRu-25, respectively, in accordance with the $Ti_3C_2T_x$ molar mass percentages of 1, 5, and 25 %.

The morphological and microstructural properties of the prepared catalysts were characterized using SEM, XRD, and XPS. Fig. 2 shows the morphological features of the pure materials, the 2D $Ti_3C_2T_x$ MXene, and the NiRu@$Ti_3C_2T_x$ composites. In the absence of $Ti_3C_2T_x$, the hydrothermal synthesis yielded aggregated pure $Ni(OH)_2$ particles with a plate-like morphology and a particle size ranging from 50 to 150 nm, Fig. 2a. Pure Ru exhibits aggregated particles with a considerably smaller particle size and a floc-like amorphous morphology, Fig. 2b. The bimetallic hybrid, pure NiRu (Fig. 2c), displays more aggregates that are similar to those observed for Ru, with a plate-like structure underneath. This suggests that Ni may act as a template, with its surface and edges serving as active sites for the growth of Ru [47]. SEM images of $Ti_3C_2T_x$ MXene reveal the 2D sheet-like structures comprising a few layers, Fig. 2d. For the NiRu@$Ti_3C_2T_x$ composites, as illustrated in Fig. 2(e-h), the MXene sheets are predominantly covered by the NiRu nanoparticles, observable on the surface and between the layers.

To further investigate the nanoscale microstructure of the pure and

Fig. 1. Schematic representation of the NiRu@Ti3C2Tx synthesis process.

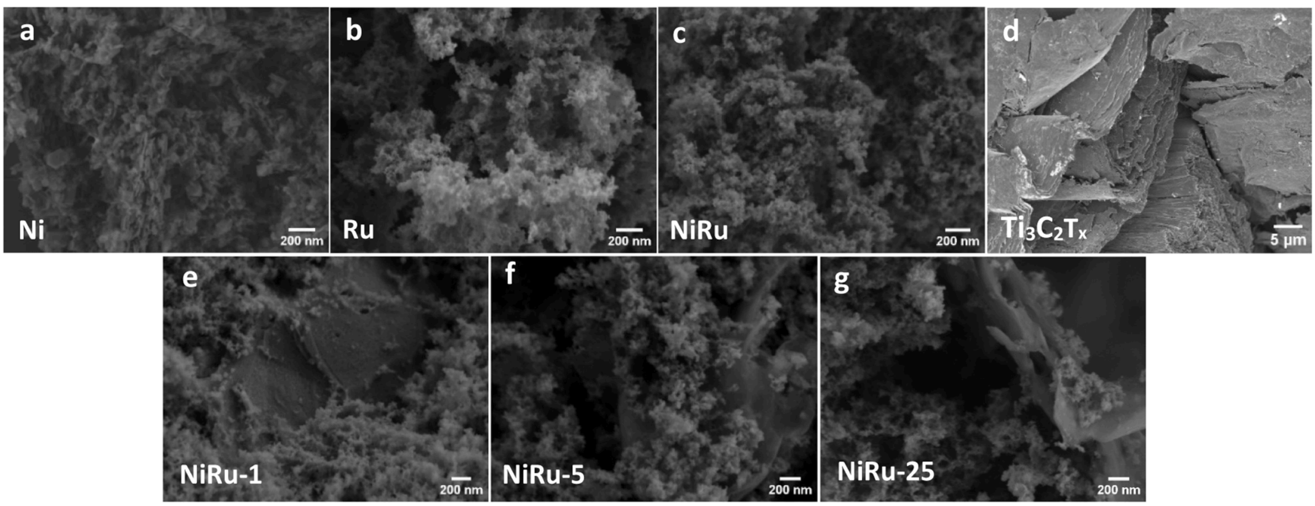

Fig. 2. SEM images of (a) pure Ni, (b) pure Ru, and (c) pure NiRu, (d) $Ti_3C_2T_x$, (e) NiRu-1, (f) NiRu-5, and (g) NiRu-25. (All SEM images are at a scale of 200 nm, except the $Ti_3C_2T_x$ which is at a scale of 5 µm. This is because the flake size of the $Ti_3C_2T_x$ is in the µm range.).

composite materials, TEM-EDX analyses were performed to determine the particle size of the pure bimetallic NiRu and its MXene composites, Figure S3. The spherical-like pure NiRu particles exhibited sizes ranging from 1 to 7 nm, with an average of 3 nm, demonstrating its ultrafine particle size. In the $Ti_3C_2T_x$ MXene and NiRu@$Ti_3C_2T_x$ composites, the MXene sheets displayed particle sizes ranging from 400 nm to microns, while the NiRu particles incorporated within the composites reached sizes of up to 10 nm. The HAADF-STEM-EDX was used to analyze the chemically functionalized surface of the $Ti_3C_2T_x$ MXene. The elemental mappings of NiRu@$Ti_3C_2T_x$ composites confirmed the successful integration of NiRu onto the $Ti_3C_2T_x$ MXene surface, showing that NiRu particles were highly dispersed and evenly distributed on the $Ti_3C_2T_x$ MXene surface.

Powder XRD measurements were conducted on the pure and composite catalysts to determine the phases present and to investigate the effects of incorporating the NiRu material with $Ti_3C_2T_x$ on the crystal structure, as illustrated in Fig. 3. The XRD patterns of pure materials are shown in Fig. 3a. All the peaks in the XRD pattern of the pure Ni can be

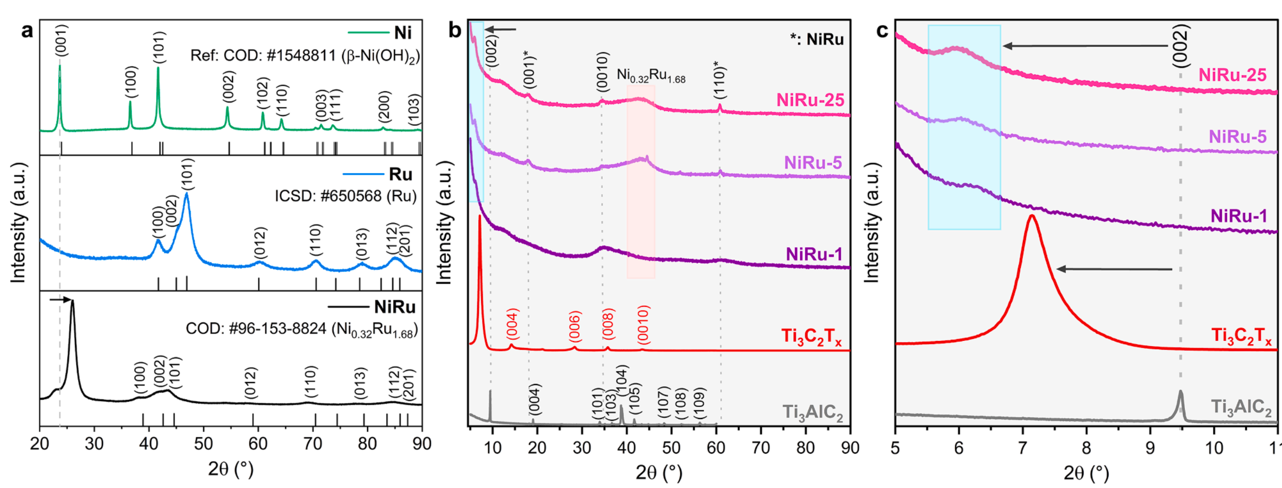

Fig. 3. X-ray diffractograms of the (a) pure Ni, Ru and NiRu, b) Ti_3AlC_2, $Ti_3C_2T_x$, and NiRu@$Ti_3C_2T_x$ composites with varying amounts of $Ti_3C_2T_x$: NiRu-1, NiRu-5, NiRu-10 and NiRu 25, (c) the magnified XRD patterns for the 2θ range from 5 to 11° from (b).

indexed to the β-$Ni(OH)_2$ (COD: #1,548,811). The XRD pattern of pure Ru exhibits a minor peak at 39°, ascribed to the Ru (100) facet, and a broadened peak around 43.5°, indicative of the Ru (002) and (101) facets (ICSD #650,568). The XRD pattern of the pure NiRu hybrid material confirms that a specific set of interplanar angles, situated at 25°, 38°, 42°, 44.5°, 51.8°, 59°, 79°, 85° and 89°, are attributed to the (001) plane of metallic Ni, and (100), (002), (101), (012), (110), (113), (112), and (201) planes of metallic Ru, respectively (COD: #96–153–8824). The (001) plane of metallic Ni exhibited a shift to higher 2θ angles, while the (100), (002), (101), (012), (110), (113), (112), and (201) planes of metallic Ru demonstrated a shift to lower 2θ angles. These findings support the conclusion that the Ni atoms have diffused into the Ru lattice. In the NiRu, Ni serves as a base for the nucleation and growth of Ru, while Ru incorporates into the Ni lattice by substituting some of the Ni sites. This structural change is supported by our XRD analysis. According to Bragg's equation ($d = \frac{\lambda}{2\sin\theta}$, where d is the interplanar distance, and λ and θ are the X-ray wavelength and Bragg angle), a shift in the (001) plane of Ni towards a higher angle indicates a reduction in d. This shift suggests that Ru may have substituted for Ni^{2+} in the NiRu lattice, as the ionic radius of Ru (0.62 Å for Ru^{4+} and 0.68 Å for Ru^{3+}) is smaller than that of Ni^{2+} (0.69 Å). Consequently, the observed shift towards higher angles aligns with the expected contraction of the lattice, confirming the successful formation of the NiRu structure. The diffraction pattern for the $Ti_3C_2T_x$ exhibits peaks at 6°, 14°, 28°, 35°, and 43°, which are in accordance with the reported patterns for $Ti_3C_2T_x$ MXene (Fig. 3b). The diffraction pattern of the $Ti_3C_2T_x$ indicates complete etching of Al layers from the Ti_3AlC_2 MAX phase, evidenced by the strong (002) and (004) reflections at 7.2° and 14.4° as well as the absence of the (104) peak and the strong (002) peak at 6°, respectively. Furthermore, the shift in the (002) peak to lower 2θ angles indicates an increase in the interplanar distance between the pure MXene layers, which provides evidence for the successful delamination of the $Ti_3C_2T_x$. In the case of the NiRu@$Ti_3C_2T_x$ composites, the (002) peak exhibited a further shift to lower 2θ angles, indicating the incorporation of pure NiRu and a consequent increase in the interplanar distance between the MXene layers (Fig. 3c).

To give insight into the surface structure and oxidation state of the pure and composite materials synthesized, XPS was carried out (Fig. 4 and Supplementary Figure S1).

The $Ni2p_{3/2}$ core level shape shows that the pure Ni material exhibits an oxidation state of Ni^{2+} [48] and is present as $Ni(OH)_2$ (Fig. 4a), in

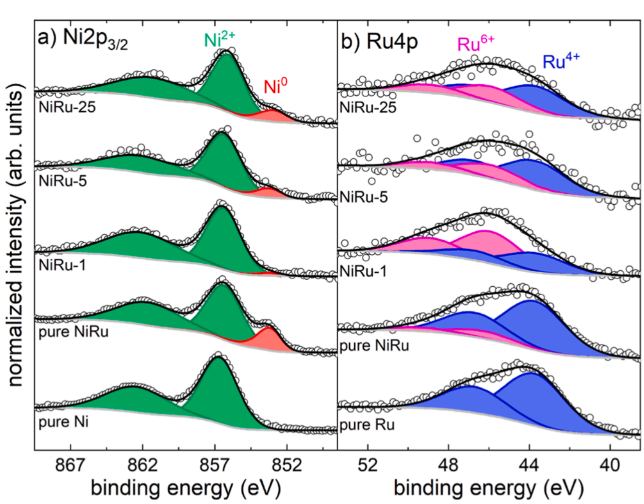

Fig. 4. a) $Ni2p_{3/2}$ and b) Ru4p X-ray photoelectron spectroscopy high resolution core level spectra of the pure and composite materials for different amounts of $Ti_3C_2T_x$ MXene. Mixture of Ni and Ru materials leads to a reduction of $Ni(OH)_2$ to metallic nickel and a further oxidation of the ruthenium oxide. The addition of small amounts of $Ti_3C_2T_x$ decreases the reduction of Ni and increases the oxidation of Ru. This effect is less pronounced for higher amounts of $Ti_3C_2T_x$.

agreement with XRD results. A Ni Auger parameter of 1698.3 eV further supports the presence of $Ni(OH)_2$ (Supplementary Figure S2) [49]. Upon addition of the Ru to obtain the pure NiRu, the oxidation state of the Ni is partly reduced to Ni metal. Interestingly, at low $Ti_3C_2T_x$ concentrations (1 and 5 %) the Ni metal content is significantly diminished, indicating that the MXene oxidizes the Ni. At 25 % $Ti_3C_2T_x$, the Ni metal content is only slightly reduced compared to the pristine NiRu.

From the XPS it is evident that upon addition of 1 % MXene to the pure NiRu, the Ni and Ru gets oxidized, Fig. 4. The rationale behind this is not entirely clear, however, it could be due to the presence of the Ti-C on the surface which is not present for the other NiRu composites.

The reduction of the Ni and Ru upon addition of 5 and 25 % $Ti_3C_2T_x$ can be supported by many studies in the literature [50]. One study by Xu and co-workers reported on the reducing effect of MXene in relation to the Fenton reaction, where a $Ti_3C_2T_x$-Fe^{3+} complex was formed through oxygen termination sites and then the breaking of Ti-C bonds [51]. This study resulted in the reduction of the Fe metal and the oxidation of the $Ti_3C_2T_x$. A second study, which is similar to the first, rationalized the reducing effect of the MXene to its termination sites e.g. OH^- sites. In that study, Wang and co-workers reported that Au metal salts were reduced to metals using no reducing agent and in the presence of MXenes only [52].

Hence utilizing the knowledge from these studies, conclusions of the reducing effect of the MXene on the NiRu can be made. In the XPS spectra form the C1s region, in Figure S1b, the Ti-C bond of the pure MXene is assigned to a peak at 281.6 eV. However, from the NiRu@$Ti_3C_2T_x$ composites, in particular NiRu-25 and NiRu-5, this Ti-C peak is no longer present. Additionally, a new peak appears at approximately 458.8 eV in the Ti2p core level, Figure S1a, for the NiRu@MXene composites due to TiO_2 formation. This change indicates that most of the Ti-C bonds undergo a reaction to form TiO_2 when NiRu is incorporated with MXene, which may have initiated with the binding of the metal oxide to the MXene termination sites. A redox reaction occurs between MXene and both Ni and Ru, where Ru^{6+} is reduced to Ru^{4+} and Ni^{2+} is reduced to Ni^0. During this process, MXene donates electrons to facilitate the reduction of Ru^{6+} and Ni^{2+} to Ru^{4+} and Ni^0, respectively, through the self-oxidation of Ti. The following mechanisms, shown in Eqs. 2-4, are proposed for these reactions:

$$Ni^{2+} + Ti_3C_2T_x \rightarrow Ni^0 + C@TiO_2 \quad \text{(Eqn 2)}$$

$$Ni^{2+} + 2e^- \xrightarrow{\text{Ti3C2}} Ni^0 \quad \text{(Eqn 3)}$$

$$Ni^0 \xrightarrow{\text{Ti3C2(OH)2}} Ni^{2+} + 2e^- \quad \text{(Eqn 4)}$$

As there is significant overlap with the Ti2p and the Ru3p regions, as well as the C1s and the Ru3d regions (Supplementary Fig. S1), these core levels are unsuitable for quantitative analysis of Ru. Therefore, the oxidation states of Ru were determined through the analysis of the Ru4p region (Fig. 4b). The Ru4p core level of the pure Ru material shows one oxidation state, Ru^{4+}, in contrast to the XRD results, which indicate that the bulk material has only one phase, metallic Ru. This can be attributed to the fact that XPS is a surface-sensitive technique and, as Ru is prone to oxidation, the surface of the pure Ru material was probably oxidized before or during the XPS measurements. In contrast, XRD is more bulk sensitive, and the bulk Ru exhibits metallic character. Upon combination with Ni to form the bimetallic NiRu material, Ru^{4+} slightly undergoes further oxidation, resulting in the emergence of a second pair of peaks at higher binding energies. Addition of small amounts of MXene to the NiRu composite leads to a strong increase of the oxidation, likely forming Ru^{6+}, which is the stable valence state of Ru in very alkaline media [9]. This phenomenon is less pronounced at higher MXene contents.

The pure $Ti_3C_2T_x$ MXene material exhibits a strong Ti-C peak in the C1s region as well as no signal from TiO_2 in the Ti2p region, which confirms the MXene structure is intact and not oxidized after the exfoliation and delamination process [53] (Supplementary Figure S1). However, after mixture with the NiRu composite the MXene gets partially oxidized and forms TiO_2, another indication for the electron transfer observed already before for the nickel and ruthenium core levels.

3.2. Electrocatalytic performance for OER

The electrocatalytic OER performance of the pure and composite materials with varying $Ti_3C_2T_x$ concentrations on industrial relevant Ni felts are illustrated in Figs. 5 and 6. First, the pure $Ti_3C_2T_x$ was tested, and the CV profile shows that the pure MXene itself is not OER active as the MXene decreases the inherent OER activity of the Ni felt support (Fig. 5a). The pure Ni material, which was confirmed by XRD and XPS to be β-$Ni(OH)_2$ phase, experiences reversible phase transformations to form its electrocatalytically active phase, β-NiOOH (Fig. 5b, A1) at 1.4 V vs. RHE [54,55].

For the pure Ru catalyst, the oxidation process is more complex in alkaline electrolyte, as Ru can exist in a variety of oxidation states with most of the compounds forming in the range of +2 to +7 (A2 and A3, Fig. 5b and c). The theoretical demonstrations by Pourbaix have shown that, in alkaline media, Ru undergoes several reactions that change its oxidation state rapidly, depending on the pH and the potential [9]. From the CV curve, Fig. 5b, the A2 peak can be assigned to the redox transition of Ru(IV) to Ru(VI), Eq. 5 [56]. Furthermore, up to potentials of 1.46 V vs. RHE, the rapid formation and decomposition of unstable green perruthanate RuO_4^- occurs, Eq. 6. This further resulted in the reduction of the RuO_4^- back to the orange ruthenate (RuO_4^{2-}) and leaching into the electrolyte, as evidence by the change in solution color, Figure S4. The further decomposition of unstable RuO_4^- phase and RuO_4^{2-} ion (dissolved) to the black hydrated dioxide $RuO_2{\cdot}2H_2O$ (solid) was observed as well for pure Ru, which could be due to the high quantity of unstable RuO_4^- phase in the solution. The potential reaction pathways for the formation of these compounds are provided in Eqs. 5 and 6:

A2: Ru(IV)/Ru(VI): $\mathbf{RuO_2} + 4OH^- \rightarrow \mathbf{RuO_4^{2-}} + 2H_2O + 2e^-$ (Eq. 5)

A3: Ru(VI)/Ru(VII): $\mathbf{RuO_4^{2-}} \rightarrow \mathbf{RuO_4^-} + e^-$ (Eq. 6)

In the case of the pure NiRu, the oxidation peak was observed at approximately 1.12 V vs. RHE (A1+A3, Fig. 5b). When compared to the pure Ni and pure Ru CV response, this A1+A3 peak becomes sharp, which is in agreement with previous reports for bimetallic NiRu oxide [57]. The electrolyte color change was less pronounced than that observed for the pure Ru, from clear to light orange, but was still present and observable for the pure NiRu. Upon collecting the electrolyte, further decomposition of the unstable RuO_4^- phase and RuO_4^{2-} ions to the black hydrated dioxide $RuO_2{\cdot}2H_2O$ was observed, as evidenced by the presence of black sediments in the electrolyte, Figure S4.

The objective behind the production of NiRu@$Ti_3C_2T_x$ composites with varying $Ti_3C_2T_x$ amounts was to examine the impact of $Ti_3C_2T_x$ MXene on the stabilization of Ru in its stable phase and the prevention of the formation of unstable Ru phases, with the ultimate goal of enhancing the high electrocatalytic activity of Ru towards OER. To understand how the MXene effected the Ru stabilization and ultimately the OER, a range of NiRu/$Ti_3C_2T_x$ composites, namely NiRu-1, NiRu-5, and NiRu-25, was also investigated. In the case of the composites, the redox transitions for both Ni and Ru were shifted to lower potentials (A1+A3, A2, Fig. 5d). The shapes of the CV curves were similar to that of NiRu/NF, particularly for NiRu-1 and NiRu-5, indicating that the NiRu material was effectively present on the MXene surface throughout the CV measurements, that is, both Ni and Ru contributing effectively to the electroactivity of the composites towards OER. The current density of the NiRu-1 was similar to that of the pure NiRu, ~100 $mA{\cdot}cm^{-2}$, while that of NiRu-5 was higher at 116 $mA{\cdot}cm^{-2}$. The current density of NiRu-25 was decreased to 60 $mA{\cdot}cm^{-2}$ as the percentage of $Ti_3C_2T_x$ increased from 5 % to 25 %. Nevertheless, the current densities, as well as the curve shapes, of pure Ni and NiRu-25 were found to be highly comparable, with NiRu-25 exhibiting Ru transitions at ~1.1 V vs. RHE. This suggests that the NiRu-25 displays Ni characteristics to a greater extent while retaining the Ru within the composite.

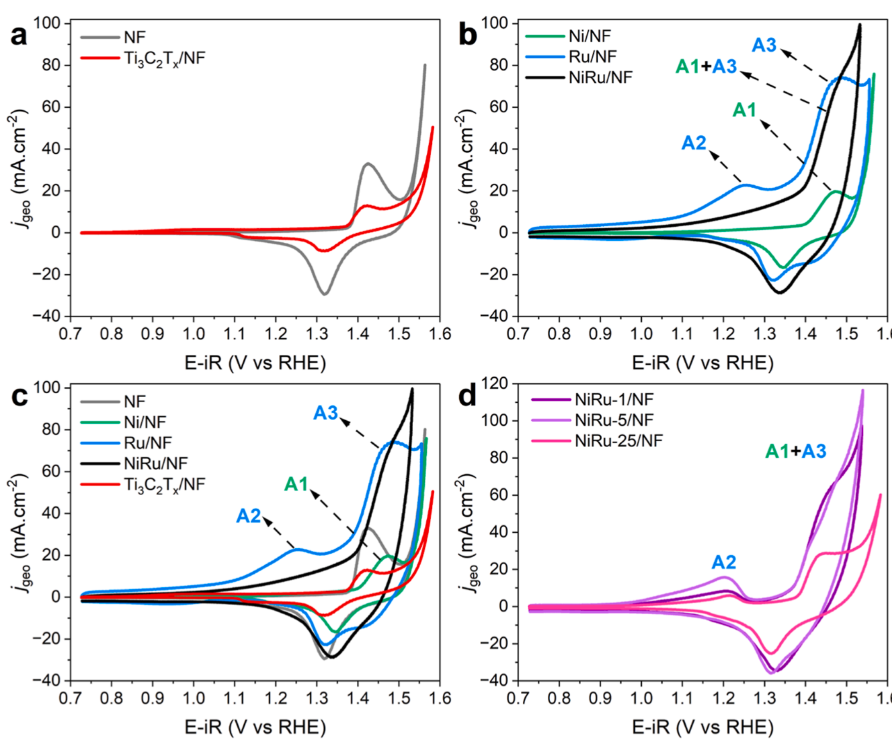

Fig. 5. iR-corrected cyclic voltammograms of (a) bare Ni felt (NF) and pure $Ti_3C_2T_x$/NF, (b) pure Ni/NF, Ru/NF, and NiRu/NF, (c) all pure materials (Ni/NF, Ru/NF, NiRu/NF, and $Ti_3C_2T_x$/NF) and bare NF, and (d) NiRu@$Ti_3C_2T_x$ composites (NiRu-1/NF, NiRu-5/NF, and NiRu-25/NF for 1 %, 5 % and 25 % $Ti_3C_2T_x$, respectively) in 1 M KOH.

The electrocatalytic OER performance of the pure materials was investigated by LSV and compared with that of NiRu@$Ti_3C_2T_x$ composites. Fig. 6 shows the LSV curves for all materials. Compared to the pure materials, the OER onset was shifted to lower overpotentials for the NiRu@$Ti_3C_2T_x$ composites, indicating a better OER activity. Among the synthesized materials, NiRu-1 and NiRu 5 exhibited the lowest onset potentials for the OER, Fig. 6. The overpotentials at 10 mA·cm^{-2} (η_{10}) for the pure materials, Ni/NF, Ru/NF, NiRu/NF, and $Ti_3C_2T_x$/NF, were observed to be 289, 294, 262, and 331 mV, respectively. The NiRu@$Ti_3C_2T_x$ composites exhibited lower η_{10} values in comparison to the pure materials, with the exception of the pure Ru, with the obtained η_{10} of 273, 276, and 303 mV for NiRu-1, NiRu-5, and NiRu-25, respectively. To illustrate the reproducibility of OER performances, a η_{10} bar chart with error bars was also provided for all materials in Fig. 6b. All of the synthesized NiRu@$Ti_3C_2T_x$ composites achieved the 100 mA·cm^{-2} benchmark, which is a requisite for scaling up these materials to electrolyzers. The η_{100} of 345, 340, and 363 mV were found for NiRu-1, NiRu-5, and NiRu-25, respectively. Notably, the NiRu-5 exhibited the same η_{100} with the pure Ni and pure Ru, and only 11 mV higher than that of pure NiRu. It is important to note that the OER activity of the NiRu@$Ti_3C_2T_x$ composites improves at higher current densities.

The Tafel slope of the pure materials and the composites were investigated to understand the relationship between the electrochemical reaction rate and the overpotential of the subjected electrocatalysts, Fig. 6c and d. The OER is a multi-step reaction and the Tafel slopes are an indication of the rate-determining step (RDS). A Tafel slope of 60 mV·dec^{-1} would suggest a chemical step for the RDS that is observed for the Ru, 1 % and 5 %, which are the optimum materials form the LSV curve in the same current density region as the Tafel plots. Hence, the Tafel analysis shows that a chemical step is favorable for these materials for the OER as it allows the materials to undergo an alternative reaction pathway to the materials with a Tafel slope of about 40 mV·dec^{-1}, which

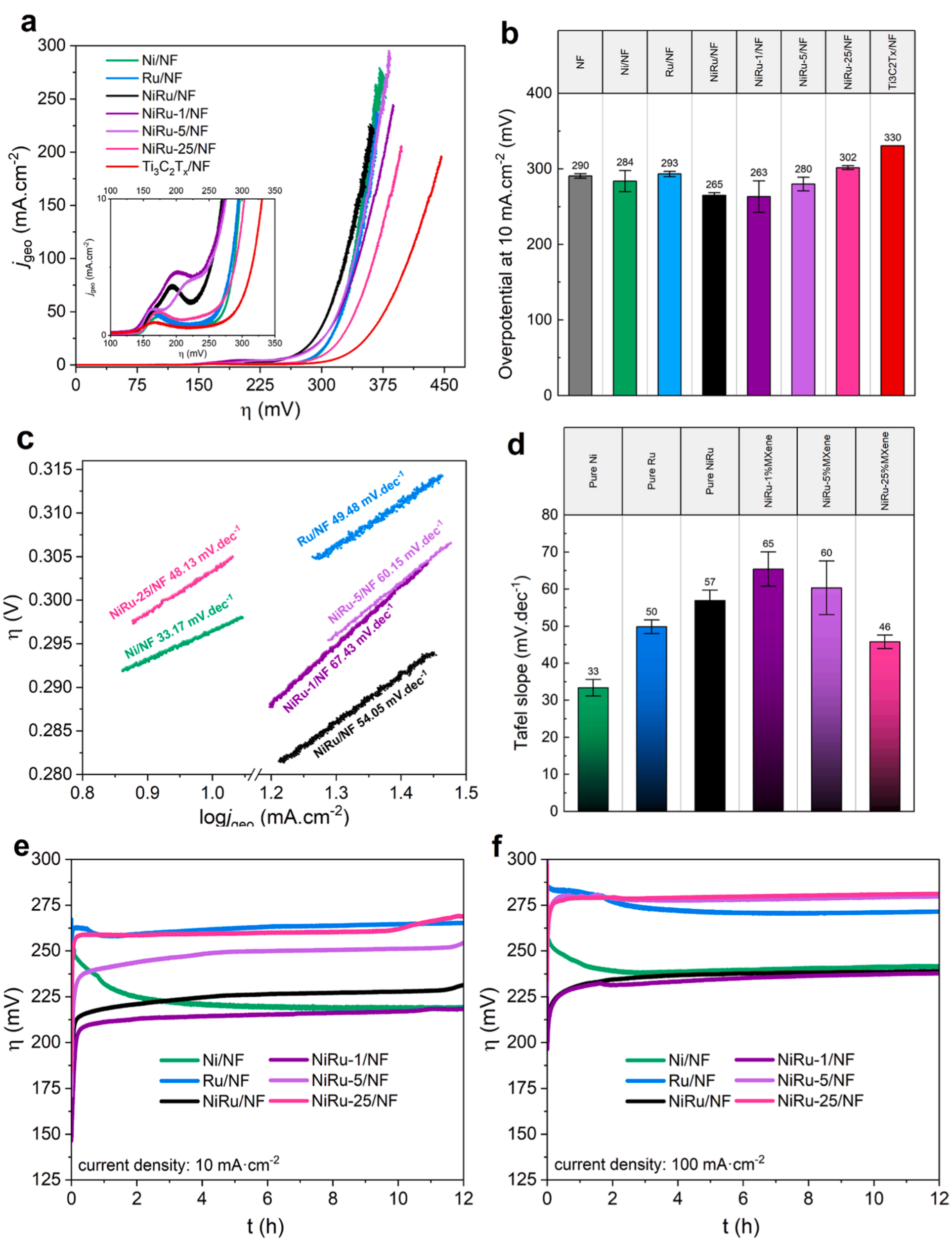

Fig. 6. (a) iR corrected LSV curves of the pure and composite materials recorded at 1 mV·s^{-1} in 1 M KOH, (b) error bar charts for the corresponding overpotentials at 10 mA·cm^{-2}, (c) Tafel slopes, (d) error bar charts for the corresponding Tafel slopes, (e) stability performance of pure materials and NiRu@$Ti_3C_2T_x$ composites at 10 mA·cm^{-2} over 12 h.

indicates the RDS is the first electron transfer step [58].

The stability of the catalyst is a crucial factor to be addressed when considering the scale-up and commercial application of the electrocatalysts. To investigate the performance of the pure materials and the NiRu@$Ti_3C_2T_x$ composites, chronopotentiometry was performed for 12 h, whereby the change in potential required to obtain a current density of 10 mA·cm^{-2} was measured (Fig. 6e). NiRu-1 exhibited the best performance with a low overpotential at 10 mA·cm^{-2} and remarkable long-term electrochemical stability for 12 h in 1 M KOH electrolyte. The initial η_{10} for NiRu-1 was 209 mV, which was then slightly increased to 218 mV after 12 h. The stability of NiRu-5 and NiRu-25 exhibited higher η_{10} than that of NiRu-1 over 12 h. However, the η_{10} were still only 254 and 269 mV after 12 h, which can be considered as high performance when compared to similar electrocatalysts, outperforming commercial RuO_2 and the similar MXene-supported catalysts [59,60].

To investigate the Fe effect on stability and overpotential values, the 1 M KOH was purified to remove the Fe following a well-known procedure [61], and additional electrochemical measurements were conducted using both the purified non-purified 1 M KOH electrolytes. The overpotentials at 100 mA·cm^{-2} after 12 h were compared under identical testing conditions and presented as Figure S5. Interestingly, when comparing the stabilities and overpotentials after 12 h, the pure NiRu and the NiRu@$Ti_3C_2T_x$ composites exhibited increased activity with reduced overpotential values in purified 1 M KOH. Furthermore, compared to 100 mA·cm^{-2}, the NiRu@$Ti_3C_2T_x$ composites demonstrated enhanced stability at 100 mA·cm^{-2}, highlighting their potential scalability for application in electrolyzers operating at high current densities. In contrast, the pure Ni exhibited a significant increase in overpotential and an altered stability profile, indicating that Fe enhances the OER activity in pure Ni, in agreement with findings from previous studies [62,63]. More detailed information on the overpotential values obtained from stability tests at 10 mA·cm^{-2} and 100 mA·cm^{-2} in both purified and as-used 1 M KOH after 1 h and 12 h is provided in Table S1.

3.3. *Influence of MXene on Ru stability*

The influence of the MXene incorporation on the stability of Ru was first identified through visual observation of the color of the solution. After the OER stability measurements, Fig. 7a, it is clear that the pure Ru has ionic leaching as the electrolyte's color changed from clear to diluted orange, and solid Ru precipitates which is observed as the black material in the vial. Moreover, Ru in the pure NiRu catalyst was entirely precipitated at the base of the vial, indicating that the Ru in the NiRu structure was unable to maintain a stable oxidation state and produced the completely black hydrated dioxide $RuO_2{\cdot}2H_2O$. For the MXene composite materials, a significant decrease in solid Ru leaching was immediately evident. It is worth noting that no black precipitate was observed in the MXene composites, with the exception of NiRu-1, which only contains a significantly less amount of black hydrated dioxide ($RuO_2{\cdot}2H_2O$) precipitate in comparison to pure Ru and pure NiRu. A distinct trend is observed in the color of the solutions, which undergo a transition from yellow to clear with an increase in the amount of MXene (Eq. (6)).

To further investigate these observations and to quantify the leaching of Ru, ICP-OES measurements were conducted on the solutions collected after the stability measurements, as shown in Fig. 7b. The ICP-OES results align precisely with the visual observations, demonstrating a clear correlation between the disolved Ru concentration and the $Ti_3C_2T_x$ MXene content. Upon increasing $Ti_3C_2T_x$ content from 1 % to 25 %, a decrease in the Ru concentration in the solution is observed. It is also notable that this leaching trend is in accordance with the observed decrease in Ru concentration as the Ti concentration increases. These findings indicate that the interaction of $Ti_3C_2T_x$ with Ru results in the formation of stable Ru compounds thus preventing the leaching of Ru in the form of $RuO_2{\cdot}xH_2O$, which could be related to the different oxidation states of Ru in the MXene composites, as observed from the XPS, Fig. 4.

To assess the potential influence of NiRu metal content variations on the observed behavior, the elemental concentrations and the Ni:Ru ratio of the synthesized materials were determined via ICP-OES, and the corresponding results were presented in Figure S6. The results reveal that the Ni:Ru ratio was consistently measured at 0.7 across all sample compositions. This confirms that the Ni:Ru ratio remains constant, independent of composition. Additionally, the data indicate a systematic increase in the MXene content as specified, while the Ni:Ru ratio remains unchanged, demonstrating the controlled experimental conditions. These findings confirm that there are no variations in the Ni or Ru metal content during the process, highlighting the specific role of MXene in enhancing the leaching behavior of Ru.

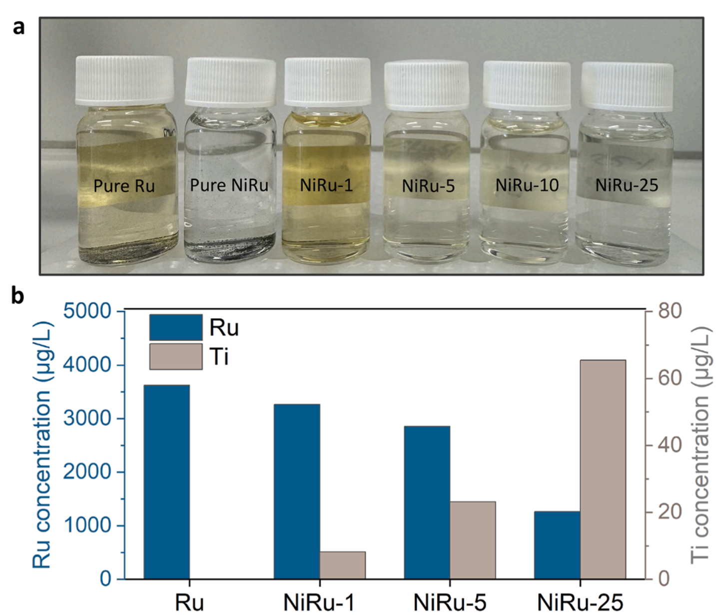

Fig. 7. (a) The electrolytes collected after the stability tests for ICP-OES measurements, showing a visual comparison of color changes (NiRu-10 is included for comparison purposes), (b) ICP-OES results for pure Ru and NiRu@$Ti_3C_2T_x$ composites.

4. Conclusion

In this study, NiRu@$Ti_3C_2T_x$ composites with varying $Ti_3C_2T_x$ contents (1 %–25 %) were successfully synthesized using a hydrothermal method. The integration of NiRu onto the $Ti_3C_2T_x$ MXene surface was confirmed through SEM, XRD, and XPS analyses, which demonstrated effective bonding and incorporation. The functionalization of $Ti_3C_2T_x$ with NiRu was evidenced to have a beneficial impact on the stabilization of Ru and the durability of the catalysts, thereby establishing an optimal equilibrium between stability and catalytic activity. NiRu-1 exhibited the best performance with an overpotential of 218 mV at 10 $mA\cdot cm^{-2}$ and remarkable long-term electrochemical stability for 12 h in unpurified 1 M KOH electrolyte.

The composites showed improved stability of Ru compared to pure Ru, as evidenced by a reduction in Ru leaching and enhanced catalytic performance in alkaline OER. Notably, the increased $Ti_3C_2T_x$ content correlated with better stabilization of Ru, attributed to the formation of stable Ru compounds and reduced leaching. These findings highlight the beneficial impact of $Ti_3C_2T_x$ functionalization on the stability and activity of metal based OER catalysts, which can be adapted to other metals and metal oxides for the stabilizing of the active sites during OER. Overall, the incorporation of $Ti_3C_2T_x$ with (transition) metal structures could potentially offer a solution to the instability of compounds, while simultaneously enhancing the electrocatalytic performance while maintaining the structural integrity.

Declaration of competing interest

The authors declare that they have no known competing financial interests or personal relationships that could have appeared to influence the work reported in this paper.

Acknowledgements

We gratefully acknowledge the Helmholtz Association's Initiative and Networking Fund (Helmholtz Young Investigator Group VH—NG-1719) for the funding. M.P.B. greatly acknowledges support from the German Federal Ministry of Education and Research in the framework of the project Catlab (03EW0015A/B). The authors would like to address particular thanks to Dr. René Schwiddessen, Dr. Michael Tovar and Dr. Klaus Schwarzburg from the X-Ray and Microscopy and Spectroscopy corelabs of the Helmholtz Zentrum Berlin for providing access to their facility and training on the equipment. The ICP-OES measurements were carried out by the "Solar Fuels Testing Facility" laboratory of the Helmholtz Energy Materials Foundry (HEMF). The authors would also like to thank Dr. Wei Zhang and Prof. Dr. Yan Lu from Helmholtz Zentrum Berlin for conducting the TEM analyses. Open Access funding enabled and organized by Projekt DEAL.

Supplementary materials

Supplementary material associated with this article can be found, in the online version, at doi:10.1016/j.electacta.2024.145529.

References

[1] IEA, "Global hydrogen review 2023". https://www.iea.org/reports/global-hydrogen-review-2023.

[2] J. Rossmeisl, A. Logadottir, J.K. Nørskov, Electrolysis of water on (oxidized) metal surfaces, Chem. Phys. 319 (1) (2005) 178–184, https://doi.org/10.1016/j.chemphys.2005.05.038, 2005/12/07/.

[3] A.J. Shih, et al., Water electrolysis, Nat. Rev. Methods Prime. 2 (1) (2022) 84, https://doi.org/10.1038/s43586-022-00164-0, 2022/10/27.

[4] Y. Lee, J. Suntivich, K.J. May, E.E. Perry, Y. Shao-Horn, Synthesis and Activities of Rutile IrO2 and RuO2 Nanoparticles for Oxygen Evolution in Acid and Alkaline Solutions, J. Phys. Chem. Lett. 3 (3) (2012) 399–404, https://doi.org/10.1021/jz2016507, 2012/02/02.

[5] M.-I. Jamesh, X. Sun, Recent progress on earth abundant electrocatalysts for oxygen evolution reaction (OER) in alkaline medium to achieve efficient water splitting – A review, J. Power. Sources. 400 (2018) 31–68, https://doi.org/10.1016/j.jpowsour.2018.07.125, 2018/10/01/.

[6] J.Z.Y. Seow, T.D. Nguyen, Electrochemically assisted synthesis of ultra-small Ru@IrOx core-shell nanoparticles for water splitting electro-catalysis, Electrochim. Acta 341 (2020) 136058, https://doi.org/10.1016/j.electacta.2020.136058, 2020/05/01/.

[7] S. Cherevko, et al., Oxygen and hydrogen evolution reactions on Ru, RuO 2, Ir, and IrO 2 thin film electrodes in acidic and alkaline electrolytes: a comparative study on activity and stability, Catal. Today 262 (2016) 170–180, https://doi.org/10.1016/j.cattod.2015.08.014.

[8] J. Llopis, M. Vázquez, Passivation of ruthenium in hydrochloric acid solution, Electrochim. Acta 11 (6) (1966) 633–640, https://doi.org/10.1016/0013-4686(66)87007-X, 1966/06/01/.

[9] M. Pourbaix, Atlas of Electrochemical Equilibria in Aqueous Solutions, NACE 1966 (1966) [Online]. Available: https://cir.nii.ac.jp/crid/1572543024422924800.

[10] S. Anantharaj, S. Kundu, S. Noda, The Fe Effect": a review unveiling the critical roles of Fe in enhancing OER activity of Ni and Co based catalysts, Nano Energy 80 (2021) 105514, https://doi.org/10.1016/j.nanoen.2020.105514. /02/01/2021.

[11] A. Karmakar, et al., Stabilization of ruthenium nanoparticles over NiV-LDH surface for enhanced electrochemical water splitting: an oxygen vacancy approach, J Mater Chem A 10 (7) (2022) 3618–3632, https://doi.org/10.1039/D1TA09627C, 10.1039/D1TA09627C.

[12] W.H. Lee, M.H. Han, Y.-J. Ko, B.K. Min, K.H. Chae, H.-S. Oh, Electrode reconstruction strategy for oxygen evolution reaction: maintaining Fe-CoOOH phase with intermediate-spin state during electrolysis, Nat. Commun. 13 (1) (2022) 605, https://doi.org/10.1038/s41467-022-28260-5, 2022/02/01.

[13] C. Liu, W. Xing, Ruthenium-based metal oxide for acidic oxygen evolution reaction: advances and challenges, Energy Lab 1 (2023), https://doi.org/10.54227/elab.20220018.

[14] K. Wang, et al., Highly active ruthenium sites stabilized by modulating electron-feeding for sustainable acidic oxygen-evolution electrocatalysis, Energy Environ. Sci. 15 (6) (2022) 2356–2365, https://doi.org/10.1039/D1EE03610F, 10.1039/D1EE03610F.

[15] Y. Xue, et al., Stabilizing ruthenium dioxide with cation-anchored sulfate for durable oxygen evolution in proton-exchange membrane water electrolyzers, Nat. Commun. 14 (1) (2023) 8093, https://doi.org/10.1038/s41467-023-43977-7, 2023/12/07.

[16] P.L. Zhai, et al., Engineering single-atomic ruthenium catalytic sites on defective nickel-iron layered double hydroxide for overall water splitting (in English), Nat. Commun. 12 (1) (2021), https://doi.org/10.1038/s41467-021-24828-9. Jul 28.

[17] Y. Zhao, et al., Redirecting dynamic structural evolution of nickel-contained RuO2 catalyst during electrochemical oxygen evolution reaction, J. Energy Chem. 69 (2022) 330–337, https://doi.org/10.1016/j.jechem.2022.01.030.

[18] M.P. Browne, H. Nolan, G.S. Duesberg, P.E. Colavita, M.E.G. Lyons, Low-overpotential high-activity mixed manganese and ruthenium oxide electrocatalysts for oxygen evolution reaction in alkaline media, ACS. Catal. 6 (4) (2016) 2408–2415, https://doi.org/10.1021/acscatal.5b02069, 2016/04/01.

[19] L.M. Salonen, D.Y. Petrovykh, Y.V. Kolen'ko, Sustainable catalysts for water electrolysis: selected strategies for reduction and replacement of platinum-group metals, Mater. Today Sustain. 11-12 (2021) 100060, https://doi.org/10.1016/j.mtsust.2021.100060. /03/01/2021.

[20] S. Zhou, et al., Engineering electrocatalytic activity in nanosized perovskite cobaltite through surface spin-state transition, Nat. Commun. 7 (1) (2016) 11510, https://doi.org/10.1038/ncomms11510, 2016/05/17.

[21] S. Peng, et al., Necklace-like Multishelled Hollow Spinel Oxides with Oxygen Vacancies for Efficient Water Electrolysis, J. Am. Chem. Soc. 140 (42) (2018) 13644–13653, https://doi.org/10.1021/jacs.8b05134, 2018/10/24.

[22] M. Liu, K.-A. Min, B. Han, L.Y.S. Lee, Interfacing or Doping? Role of Ce in Highly Promoted Water Oxidation of NiFe-Layered Double Hydroxide, Adv. Energy Mater. 11 (33) (2021) 2101281, https://doi.org/10.1002/aenm.202101281, 2021/09/01.

[23] W. Li, D. Xiong, X. Gao, L. Liu, The oxygen evolution reaction enabled by transition metal phosphide and chalcogenide pre-catalysts with dynamic changes, Chem Commun 55 (60) (2019) 8744–8763, https://doi.org/10.1039/C9CC02845E, 10.1039/C9CC02845E.

[24] C. Dong, et al., Rational design of cobalt–chromium layered double hydroxide as a highly efficient electrocatalyst for water oxidation, J Mater Chem A 4 (29) (2016) 11292–11298, https://doi.org/10.1039/C6TA04052G, 10.1039/C6TA04052G.

[25] W. Wu, Y. Wu, D. Zheng, K. Wang, Z. Tang, Ni@Ru core-shell nanoparticles on flower-like carbon nanosheets for hydrogen evolution reaction at All-pH values, oxygen evolution reaction and overall water splitting in alkaline solution, Electrochim. Acta 320 (2019), https://doi.org/10.1016/j.electacta.2019.134568.

[26] M. You, et al., In-situ growth of ruthenium-based nanostructure on carbon cloth for superior electrocatalytic activity towards HER and OER, Appl. Catal. B Environ. 317 (2022) 121729, https://doi.org/10.1016/j.apcatb.2022.121729, 2022/11/15/.

[27] C. Gao, et al., Enhanced cobalt-based catalysts through alloying ruthenium to cobalt lattice matrix as an efficient catalyst for overall water splitting, Electrochim. Acta 327 (2019), https://doi.org/10.1016/j.electacta.2019.134958.

[28] D. Tyndall, et al., Understanding the effect of MXene in a TMO/MXene hybrid catalyst for the oxygen evolution reaction, NPJ. 2D. Mater. Appl. 7 (1) (2023) 15, https://doi.org/10.1038/s41699-023-00377-1, 2023/03/10.

[29] J. Liu, et al., Nickel-ruthenium nanoalloy encapsulated in mesoporous carbon as active electrocatalysts for highly efficient overall water splitting in alkaline solution, Electrochim. Acta 334 (2020) 135653, https://doi.org/10.1016/j.electacta.2020.135653, 2020/02/20/.

[30] B. Anasori, M. Naguib, E. Guest, Two-dimensional MXenes, MRS Bulletin 48 (3) (2023) 238–244, https://doi.org/10.1557/s43577-023-00500-z, 2023/03/01.
[31] M. Naguib, M.W. Barsoum, Y. Gogotsi, Ten years of progress in the synthesis and development of MXenes, Advanced Materials 33 (39) (2021) 2103393, https://doi.org/10.1002/adma.202103393, 2021/10/01.
[32] M. Sokol, V. Natu, S. Kota, M.W. Barsoum, On the Chemical Diversity of the MAX Phases, Trends. Chem. 1 (2) (2019) 210–223, https://doi.org/10.1016/j.trechm.2019.02.016, 2019/05/01/.
[33] N. Li, et al., Synergistic phosphorized NiFeCo and MXene interaction inspired the formation of high-valence metal sites for efficient oxygen evolution, J. Mater. Sci. Technol. 106 (2022) 90–97, https://doi.org/10.1016/j.jmst.2021.08.007.
[34] T. Rasheed, et al., Bifunctional electrocatalytic water splitting augmented by cobalt-nickel-ferrite NPs-supported fluoride-free MXene as a novel electrocatalyst, Fuel 346 (2023) 128305, https://doi.org/10.1016/j.fuel.2023.128305, 2023/08/15/.
[35] I.H. Sajid, M.Z. Iqbal, S. Rizwan, Recent advances in the role of MXene based hybrid architectures as electrocatalysts for water splitting, RSC. Adv. 14 (10) (2024) 6823–6847, https://doi.org/10.1039/D3RA06725D, 10.1039/D3RA06725D.
[36] X. Liu, et al., Adjusting surface electron density of heterostructured NiCo LDH/MXene/NF material to improve its electrocatalytic performance in hydrogen evolution reaction, Int. J. Hydrogen. Energy 67 (2024) 192–199, https://doi.org/10.1016/j.ijhydene.2024.04.171, 2024/05/20/.
[37] L. Yan, D. Song, J. Liang, X. Li, H. Li, Q. Liu, Fabrication of highly efficient Rh-doped cobalt–nickel-layered double hydroxide/MXene-based electrocatalyst with rich oxygen vacancies for hydrogen evolution, J. Colloid. Interface Sci. 640 (2023) 338–347, https://doi.org/10.1016/j.jcis.2023.02.113, 2023/06/15/.
[38] B. Schmiedecke, et al., Enhancing the oxygen evolution reaction activity of CuCo based hydroxides with V2CTx MXene, J Mater Chem A (2024), https://doi.org/10.1039/D4TA02700K, 10.1039/D4TA02700K.
[39] J. Chen, et al., Progress in MXene-based catalysts for oxygen evolution reaction, Electron 2 (1) (2024) e17, https://doi.org/10.1002/elt2.17, 2024/02/01.
[40] M.P. Browne, D. Tyndall, V. Nicolosi, The potential of MXene materials as a component in the catalyst layer for the Oxygen Evolution Reaction, Curr. Opin. Electrochem. 34 (2022) 101021, https://doi.org/10.1016/j.coelec.2022.101021. /08/01/2022.
[41] A. VahidMohammadi, J. Rosen, Y. Gogotsi, The world of two-dimensional carbides and nitrides (MXenes), Science (1979) 372 (6547) (2021) eabf1581, https://doi.org/10.1126/science.abf1581, 2021/06/11.
[42] C. Hao, et al., Interface-coupling of CoFe-LDH on MXene as high-performance oxygen evolution catalyst, Mater. Today Energy 12 (2019) 453–462, https://doi.org/10.1016/j.mtener.2019.04.009, 2019/06/01/.
[43] C. Kaplan, et al., Effect of the synthesis route and Co Coverage on Co /Ti3C2Tx materials for the oxygen evolution reaction, English, Electrochim. Acta 490 (Jun 20 2024), https://doi.org/10.1016/j.electacta.2024.144269.
[44] Y. Lu, D. Fan, Z. Chen, W. Xiao, C. Cao, X. Yang, Anchoring Co3O4 nanoparticles on MXene for efficient electrocatalytic oxygen evolution, Sci Bull 65 (6) (2020) 460–466, https://doi.org/10.1016/j.scib.2019.12.020, 2020/03/30/.
[45] X. Yu, et al., Immobilizing bimetallic RuCo nanoalloys on few-layered MXene as a robust bifunctional electrocatalyst for overall water splitting, Chem. Eur. J. 30 (8) (2024) e202303524, https://doi.org/10.1002/chem.202303524, 2024/02/07.
[46] N. Fairley, et al., Systematic and collaborative approach to problem solving using X-ray photoelectron spectroscopy, Appl. Surf. Sci. Adv. 5 (2021) 100112, https://doi.org/10.1016/j.apsadv.2021.100112. /09/01/2021.
[47] J.B. Ding, Q. Shao, Y.G. Feng, X.Q. Huang, Ruthenium-nickel sandwiched nanoplates for efficient water splitting electrocatalysis (in English), Nano Energy 47 (May 2018) 1–7, https://doi.org/10.1016/j.nanoen.2018.02.017.
[48] M.C. Biesinger, B.P. Payne, A.P. Grosvenor, L.W.M. Lau, A.R. Gerson, R.S.C. Smart, Resolving surface chemical states in XPS analysis of first row transition metals, oxides and hydroxides: Cr, Mn, Fe, Co and Ni, Appl. Surf. Sci. 257 (7) (2011) 2717–2730, https://doi.org/10.1016/j.apsusc.2010.10.051. /01/15/2011.
[49] M.C. Biesinger, L.W.M. Lau, A.R. Gerson, R.S.C. Smart, The role of the Auger parameter in XPS studies of nickel metal, halides and oxides, Physical Chemistry Chemical Physics 14 (7) (2012) 2434–2442, https://doi.org/10.1039/C2CP22419D, 10.1039/C2CP22419D.
[50] Q. Zhang, et al., Metal/MXene composites via in situ reduction, Nat. Synth. (2024), https://doi.org/10.1038/s44160-024-00660-z, 2024/10/04.
[51] S. Xu, et al., Ti3C2 MXene promoted Fe3+/H2O2 fenton oxidation: comparison of mechanisms under dark and visible light conditions, J. Hazard. Mater. 444 (2023) 130450, https://doi.org/10.1016/j.jhazmat.2022.130450, 2023/02/15/.
[52] Z. Zheng, et al., In situ reduced MXene/AuNPs composite toward enhanced charging/discharging and specific capacitance, Journal of Advanced Ceramics 10 (5) (2021) 1061–1071, https://doi.org/10.1007/s40145-021-0491-0, 2021/10/01.
[53] L.-Å. Näslund, P.O.Å. Persson, J. Rosen, X-ray Photoelectron spectroscopy of Ti3AlC2, Ti3C2Tz, and TiC provides evidence for the electrostatic interaction between laminated layers in MAX-phase materials, J. Phys. Chem. C 124 (50) (2020) 27732–27742, https://doi.org/10.1021/acs.jpcc.0c07413, 2020/12/17.
[54] I.J. Godwin, M.E.G. Lyons, Enhanced oxygen evolution at hydrous nickel oxide electrodes via electrochemical ageing in alkaline solution, Electrochem. commun. 32 (2013) 39–42, https://doi.org/10.1016/j.elecom.2013.03.040.
[55] S.R. Mellsop, A. Gardiner, B. Johannessen, A.T. Marshall, Structure and transformation of oxy-hydroxide films on Ni anodes below and above the oxygen evolution potential in alkaline electrolytes, Electrochim. Acta 168 (2015) 356–364, https://doi.org/10.1016/j.electacta.2015.04.020.
[56] K.A. Stoerzinger, R.R. Rao, X.R. Wang, W.T. Hong, C.M. Rouleau, Y. Shao-Horn, The role of Ru redox in pH-dependent oxygen evolution on rutile ruthenium dioxide surfaces, Chem. 2 (5) (2017) 668–675, https://doi.org/10.1016/j.chempr.2017.04.001, 2017/05/11/.
[57] I.J. Godwin, R.L. Doyle, M.E.G. Lyons, The Mechanism of oxygen reactions at porous oxide electrodes: III. water oxidation catalysis at RuO2/NiO mixed oxide electrodes, J. Electrochem. Soc. 161 (9) (2014) F906, https://doi.org/10.1149/2.0761409jes, 2014/06/12.
[58] R.L. Doyle, I.J. Godwin, M.P. Brandon, M.E.G. Lyons, Redox and electrochemical water splitting catalytic properties of hydrated metal oxide modified electrodes, Physical Chem. Chem. Phys. 15 (2013) 13737–13783, https://doi.org/10.1039/C3CP51213D.
[59] J. Li, et al., Collaborative interface optimization strategy guided ultrafine RuCo and MXene heterostructure electrocatalysts for efficient overall water splitting, ACS. Nano 17 (11) (2023) 10947–10957, https://doi.org/10.1021/acsnano.3c02956, 2023/06/13.
[60] M.Z. Yu, S. Zhou, Z.Y. Wang, J.J. Zhao, J.S. Qiu, Boosting electrocatalytic oxygen evolution by synergistically coupling layered double hydroxide with MXene (in English), Nano Energy 44 (2018) 181–190, https://doi.org/10.1016/j.nanoen.2017.12.003.
[61] L. Trotochaud, S.L. Young, J.K. Ranney, S.W. Boettcher, Nickel–Iron Oxyhydroxide Oxygen-Evolution Electrocatalysts: the Role of Intentional and Incidental Iron Incorporation, J. Am. Chem. Soc. 136 (18) (2014) 6744–6753, https://doi.org/10.1021/ja502379c, 2014/05/07.
[62] S. Anantharaj, S. Kundu, S. Noda, The Fe Effect": a review unveiling the critical roles of Fe in enhancing OER activity of Ni and Co based catalysts, Nano Energy 80 (2021) 105514, https://doi.org/10.1016/j.nanoen.2020.105514. /02/01/2021.
[63] M.T. de Groot, Alkaline water electrolysis: with or without iron in the electrolyte? Curr. Opin. Chem. Eng. 42 (2023) 100981 https://doi.org/10.1016/j.coche.2023.100981, 2023/12/01/.